

<https://doi.org/10.1038/s41524-024-01267-w>

# High-throughput approach to explore cold metals for electronic and thermoelectric devices

Check for updates

Ligong Zhang<sup>1</sup> & Fei Liu<sup>1,2</sup>

Cold metals with an energy gap around the Fermi level have been shown a great potential for reducing the power dissipation of transistors and diodes. However, only a limited number of 2D cold metals have been studied. In this work, we explored 3D cold metals through a systematic material search and found 252 types in the database. We performed first-principles calculations to investigate the conductance and work functions of 30 cold metals for material selection. Additionally, we studied the thermoelectric properties of four typical cold metals, which possess much larger Seebeck coefficients and figure-of-merits than conventional metals, by one and two orders of magnitude, respectively. Specifically, we constructed a monolayer MoS<sub>2</sub> transistor with a cold metal contact of ZrRuSb. Our quantum transport simulations indicate that cold metal contacted MoS<sub>2</sub> FETs exhibit a subthreshold swing smaller than 60 mV decade<sup>-1</sup> over four decades, and on-state currents over 1 mA μm<sup>-1</sup> are achieved at a supply voltage of 0.5 V. Our research provides a theoretical foundation and material basis for exploring 3D cold metals in developing electronic and thermoelectric devices.

Metals play a crucial role in electronic and thermoelectric devices due to their excellent electrical and thermal conductivity. Metals such as aluminum, copper, and gold are commonly used for contact and interconnects due to their excellent electrical conductivity, low resistance, and ease of fabrication<sup>1,2</sup>. Reducing materials to two-dimensional (2D) structures can lead to exotic properties distinct from their bulk counterparts, such as graphene<sup>3</sup>, transition metal dichalcogenides<sup>4</sup>, and MXenes<sup>5</sup>. It is interesting that there are 2D metals with an intrinsic energy gap around the Fermi levels, such as 2D 2H MX<sub>2</sub> (M = Nb, Ta; X = S, Se Te)<sup>6,7</sup>. Such properties are different from conventional metals and can be applied to filter high-energy electrons for cold electron injection<sup>7</sup>. Therefore, these materials are named as cold metals and were proposed to realize steep slope switching<sup>7</sup>. When these materials are used as the metal contact of the Schottky diode, an ideality factor as small as 0.17 is achieved<sup>8</sup>. Giant NDR can also be obtained with promising on-state current using cold metals<sup>8–10</sup>. 2D cold metals, while exhibiting exotic properties, tend to degrade upon exposure to the environment<sup>11</sup>. Moreover, the study of cold metals has thus far been limited to a select few 2D materials and their electronic properties. A pertinent question that arises is whether three-dimensional (3D) cold metals exist in nature.

Metals are one of the components of thermoelectric devices, which convert heat directly into electricity or vice versa through the Seebeck

effect<sup>12,13</sup>. However, metals usually have high thermal conductivity, which limits their use in thermoelectric devices due to their low thermoelectric efficiency. Metal alloys can be applied to improve thermoelectric performance<sup>14</sup>. Different from conventional metals, cold metals are similar to heavily-doped semiconductors. It has been shown that thermoelectric properties can be effectively improved in doped semiconductors<sup>15,16</sup>. Therefore, cold metals may have greater potential in thermoelectric devices.

In this work, we performed a comprehensive search for bulk cold metals and developed a fully automated search algorithm by scanning the material database. A database search reveals that thousands of metallic materials have an energy gap around the Fermi level. To meet device applications, the energy difference between the Fermi level and energy gap edge should be within 0.5 eV, and 252 kinds of cold metals are screened. The electronic and thermoelectric properties of four typical cold metals are investigated by the first-principles calculations. It is shown that these cold metals are dynamically stable and have excellent thermoelectric and electronic properties. The Power factor (PF) of CoSi can reach 10 mW m<sup>-1</sup> K<sup>-2</sup> at 700 K. The figure-of-merit  $zT$  of Sr<sub>5</sub>Pb<sub>3</sub>F can reach 0.6 at 1000 K. Except for the good thermoelectric properties, steep slope field effect transistors (FETs) with a 3D cold metal source are investigated and show promising device performance of sub-60 mV decade<sup>-1</sup> switching over four decades and on-state over 10<sup>3</sup> μA μm<sup>-1</sup>.

<sup>1</sup>School of Integrated Circuits, Peking University, Beijing 100871, China. <sup>2</sup>Beijing Advanced Innovation Center for Integrated Circuits, Beijing 100871, China.

e-mail: feiliu@pku.edu.cn

## Results

### Cold metal Screening

In recent years, high-throughput screening has been widely applied in material research and has been an important method for studying new materials<sup>17–22</sup>. We systematically searched for 3D cold metals based on the materials project (MP) database with 133,693 materials<sup>23</sup>. Two selection criteria based on known properties have to be satisfied to identify 3D cold metals: (1) the metallic materials should have an energy gap around the Fermi level within a reasonable energy region; (2) the materials have been experimentally fabricated before. The screening process is schematically shown in Fig. 1a. We first identified 11,789 stable metallic materials from the database. The key difference between cold metals and normal metals is the energy gap above or below the Fermi level, which can effectively filter high-energy carriers. In addition, the band edge of the energy gap is an essential factor. If the energy gap is far from the Fermi level, the properties of cold metals are closer to normal metals. Therefore, we identify those cold metals with an energy difference of 50 meV to 500 meV between the energy gap edge and the Fermi level. For the p-type/n-type cold metal with a gap above/below the Fermi level which is similar to the p-doped/n-doped semiconductor, we use  $E_{CD}/E_{VD}$  to describe the energy difference as shown in Fig. 1b, c. There are also np-type cold metals with a gap above the Fermi level and another gap below the Fermi level as shown in Fig. 1d. Those ferromagnetic cold metals are classified in Supplementary Fig. 2. The  $E_{CD}$  and  $E_{VD}$  cannot be obtained directly from the MP database. We analyzed the band structure provided by the MP database and got the energy gap edge to calculate the  $E_{CD}$  and  $E_{VD}$ . To confirm that screened materials are harmless and not hypothetical, we select those materials without radioactive elements and occurring in the Inorganic Crystal Structure Database (ICSD). At last, 252 kinds of cold metal are obtained.

We analyzed the elemental composition of these cold metals in a periodic table as shown in Supplementary Fig. 1. These cold metals have a total of 68 elements. The Ir element in transition metal, Eu, Yb in lanthanide elements, and F, Cl in halogens appear more frequently in cold metals. At the same time, there is a high abundance of oxygenated compounds, which should be the focus of further research due to the possible compatibility with the complementary metal oxide semiconductor (CMOS) process. We classify these cold metals by several species, crystal system, and the energy difference between the energy gap edge and the Fermi level in Supplementary Fig. 1. There are 115 kinds of p-type cold metals as listed in Supplementary Table 1. Supplementary Table 2 lists 56 kinds of n-type cold metals. 81 kinds of cold metals not only have an energy gap above the Fermi level but also have an energy gap below the Fermi level (Supplementary Table 3). We selected 10 kinds of materials from each of the three types of cold metals and calculated their conductance and work function as shown in

Fig. 2, by first-principles calculations, using the Vienna ab initio simulation package (VASP)<sup>24,25</sup>. Details of these 30 cold metals, such as atomistic structures, space groups, and band structures, are included in Supplementary Table 4. The conductance is calculated by the semi-classical Boltzmann theory with the relaxation time approximation using BoltzTrap2 code<sup>26</sup>. The electrical conductivity is linearly determined by the constant relaxation time within the relaxation time approximation, given by<sup>26</sup>:

$$\sigma(\mu; T) = q^2 \tau_0 \int \int \sum_b v_{b,k} \otimes v_{b,k} \delta(\epsilon - \epsilon_{b,k}) \left( -\frac{\partial f^{(0)}(\epsilon; \mu, T)}{\partial \epsilon} \right) \frac{dk}{8\pi^3} d\epsilon \quad (1)$$

Where  $v_{b,k}$  is the group velocities of electrons of the band index  $b$ ,  $f^{(0)}$  is the Fermi distribution function. To estimate the conductance of these cold metals, we choose a relaxation time  $\tau = 30$  fs, which is an estimated value according to the normal metals such as Cu and Au<sup>27,28</sup>. The conductance of these cold metals is shown in Fig. 2a, b, c. All these cold metals have conductance smaller than  $10 \times 10^6$  S m<sup>-1</sup>, which is lower than conventional metals due to the band gap near the Fermi level. The estimated value is an evaluation of the conductance of cold metals. The more precise conductance needs to consider electron-phonon coupling and further calculation. ZrRuSb, RhS<sub>2</sub>, and Tl<sub>2</sub>WCl<sub>6</sub> have the largest conductance among each kind of cold metal in Fig. 2a–c. Work function is important for optimizing contact resistance between metal and semiconductor for device applications. To identify the promising materials, the band alignments of these cold metals and typical semiconductors are shown in Fig. 2d. It can be found that the work function ranges from  $-4.92$  eV to  $-2.98$  eV, from  $-6.44$  eV to  $-2.69$  eV, and from  $-6.46$  eV to  $-3.29$  eV for n-type, p-type, and np-type cold metals, respectively. Therefore, it is possible to realize Ohmic contact by using cold metal contacts for both n-type and p-type transistors. For example, ZrRuSb with high conductance has a work function of  $-3.6$  eV, which is larger than the conduction band edges of Si and monolayer MoS<sub>2</sub> in Fig. 2d. Therefore, such a material can be applied to realize low contact resistance in n-type transistors.

### Electronic and thermoelectric properties

In particular, we studied the electronic and thermoelectric properties of four typical cold metal materials by first-principles calculations. These materials include ZrRuSb (F-43 m), RbCu<sub>4</sub>S<sub>3</sub> (P4/mmm), CoSi (P2<sub>1</sub>/3), and Sr<sub>5</sub>Pb<sub>3</sub>F (I4/mcm), as shown in Fig. 3a. The structures are confirmed and consistent with the experiment results<sup>29–32</sup>. The four materials have typical band structures of cold metals with a band gap around the Fermi level in Fig. 3b–e. It is noted that Sr<sub>5</sub>Pb<sub>3</sub>F is ferromagnetic with spin-polarized states around

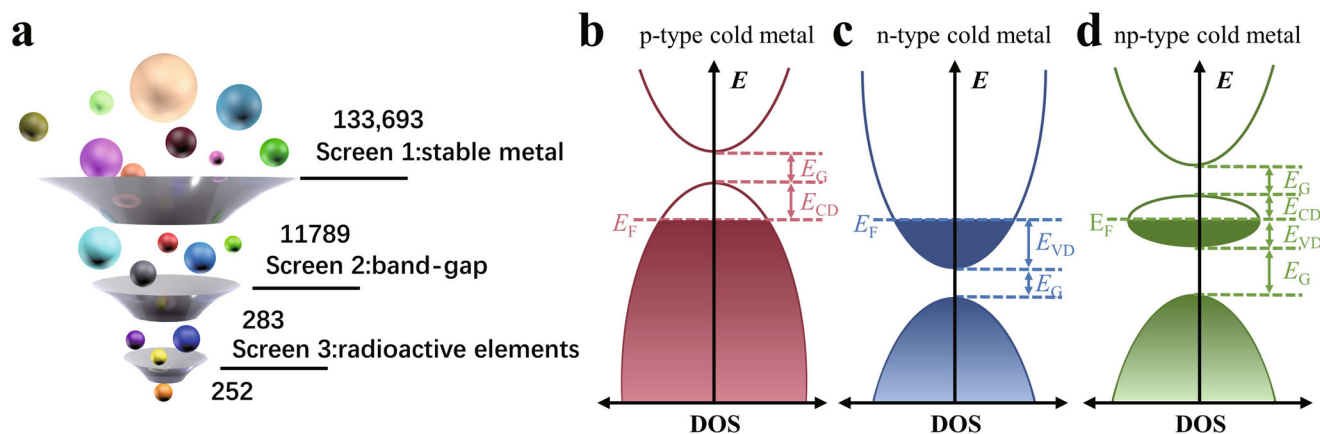


**Fig. 1 | Flow chart and Schematic representation of the density of states (DOS) of cold metal.** **a** Flow chart of material screening for cold metals. Schematic band structures of **b** p-type, **c** n-type, and **d** np-type cold metals. P-type and n-type cold

metals can be used to realize n-type and p-type steep slope transistors. While, np-type cold metal can be applied in both n-type and p-type devices.

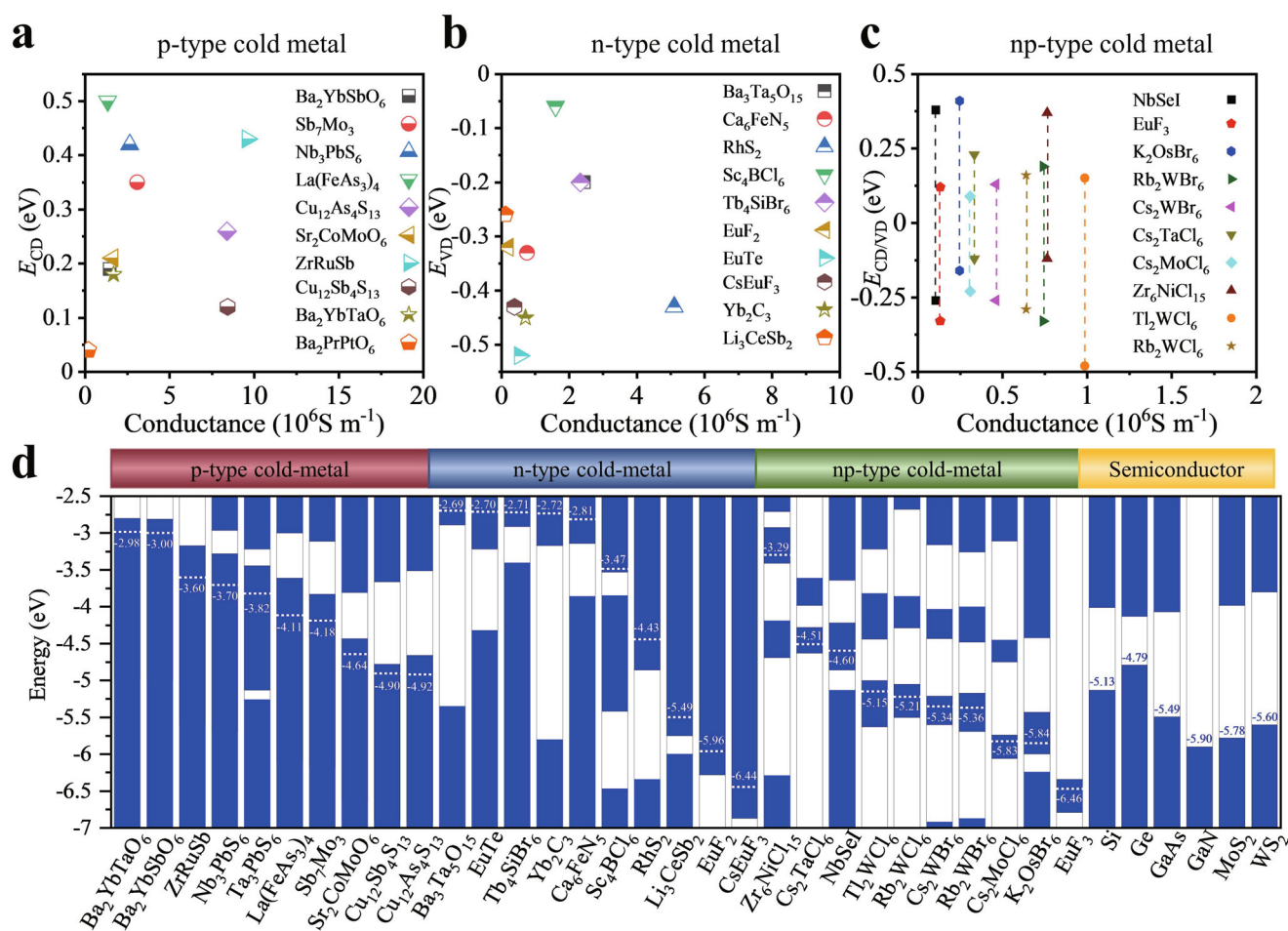


**Fig. 2** |  $E_{CD/VD}$  and work function of cold metals. **a** Conductance vs  $E_{CD}$  for p-type cold metals. **b** Conductance vs  $E_{VD}$  for n-type cold metals. **c** Conductance vs  $E_{CD}$  and  $E_{VD}$  for np-type cold metals. **d** Band alignments for different types of cold metals and

typical semiconductors. The dashed lines indicate the Fermi levels. The blue and white areas represent allowed and forbidden bands, respectively.

the Fermi level. The phonon spectra of these materials are shown in Fig. 3b–e. There is no imaginary frequency in the phonon spectrum, which indicates that these materials are dynamically stable. The projected band structure and DOS were calculated and the results are shown in Supplementary Fig. 3.

Considering the band structure of cold metals, cold metals are similar to heavily-doped semiconductors. In semiconductors, such as silicon and germanium, all valence electrons participate in covalent bonding, resulting in the presence of an energy gap that must be overcome to enable the movement of charge carriers. N-type semiconductors are achieved through the utilization of dopants such as phosphorus or arsenic, which possess five valence electrons, one more than the host semiconductor material (e.g., silicon or germanium). Conversely, p-type semiconductors are created by introducing elements like boron or gallium, which have three valence electrons. These dopants introduce “holes” within the crystal lattice, facilitating the absorption of electrons from neighboring atoms and giving rise to mobile positive charge carriers.

In contrast, cold metals naturally exhibit a higher density of mobile carriers due to the absence or excess of valence electrons. For instance, certain ternary semi-heusler compounds, such as ABX (A = Ti, Zr, Hf, V, Nb; B = Fe, Co, Ir, Ni, Pt; X = Sn, Sb), featuring 18 valence electrons, demonstrate semiconductor behavior<sup>33,34</sup>. Conversely, compounds with 17 valence electrons, including ZrRuSb, TiIrSn, TiCoSn, and TiFeSb, behave as cold metals, characterized by a band gap above the Fermi level resulting from the absence of valence electrons. Similarly, the compound TiNiSb, possessing 19 valence electrons, functions as a cold metal with a band gap

below the Fermi level. Analogous considerations can be extended to other cold metals.

We also perform the hybrid functional calculation to evaluate the band structures of 30 kinds of cold metals. The band structures calculated by HSE06 are shown in Supplementary Fig. 4 to Supplementary Fig. 8. For those materials with *f* electrons, the DFT calculation with simple pseudopotential may not be accurate<sup>35,36</sup>. Specifically, our HSE06 calculations for *f*-electron materials, such as EuF<sub>2</sub> and EuF<sub>3</sub>, reveal them to be semiconductors, contrary to the cold metal classification obtained from simple PBE calculations. In contrast, most *d*-electron materials exhibit consistent cold metal properties. However, when examining np-type cold metals with isolated bands around the Fermi energy, HSE06 calculations often yield dissimilar results compared to PBE calculations. Notably, the primary advantage of HSE06 calculations lies in accurately determining the band gap of semiconductors. It is worth noting that the HSE06 method may introduce slight inaccuracies around the Fermi level, and tends to overestimate the magnetic moments of transition metals<sup>37</sup>. These inaccuracies can potentially influence the classification of a material as a metal or a semiconductor. Consequently, given the burgeoning interest in cold metals, further research is critical to confirm their properties.

To get more accurate electronic and thermoelectric transport properties, we calculated the relaxation time of four cold metal materials with density functional perturbation theory (DFPT) and maximally localized Wannier functions (MLWFs) by EPW code in Quantum ESPRESSO<sup>38,39</sup>. The lattice thermal conductivity is calculated by phono3py<sup>40,41</sup>. Conductance, thermal conductance, Seebeck coefficient, figure-of-merit  $zT$ , and

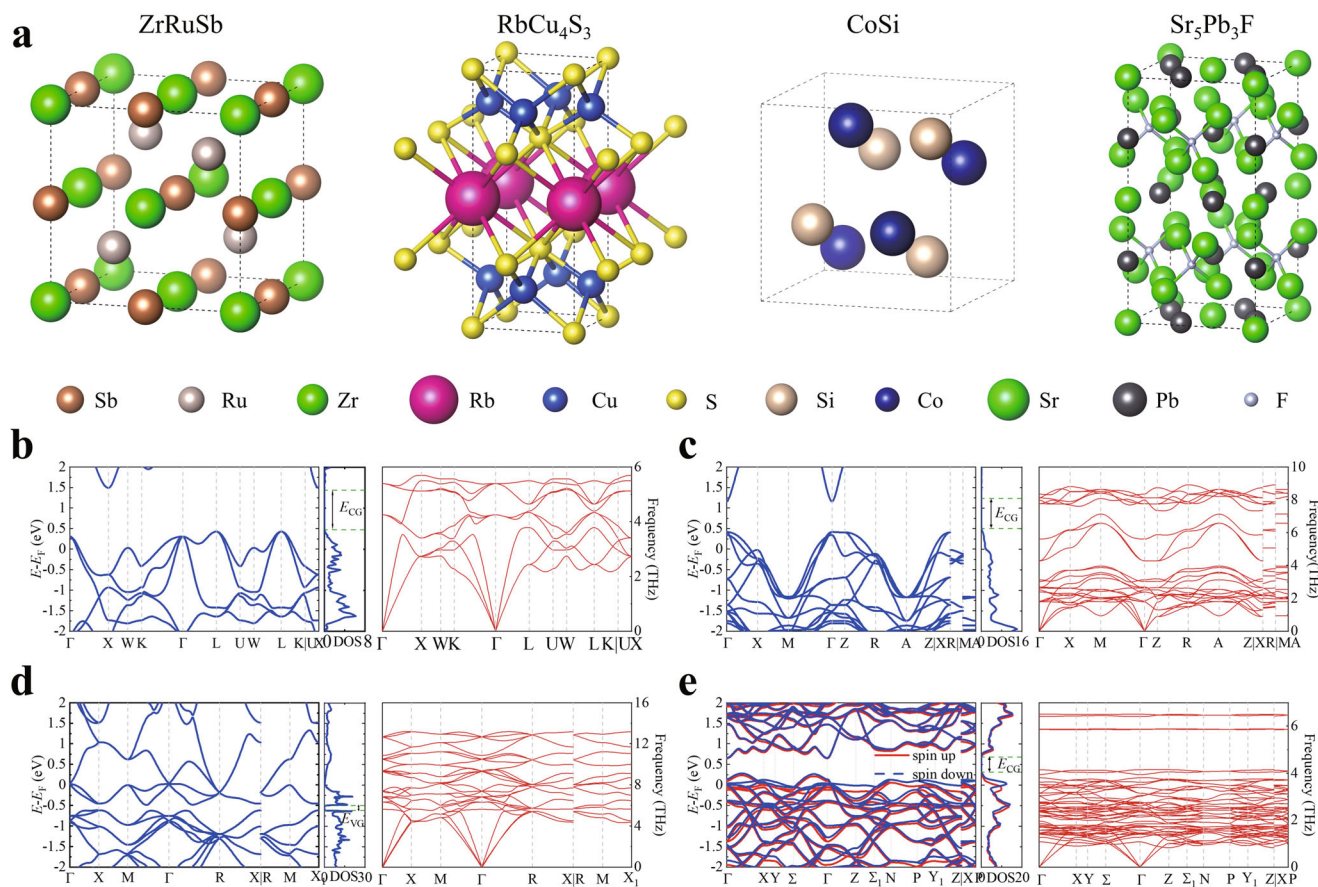


**Fig. 3 | Crystal structures, band structures, density of states (DOS), and phonon spectra of four kinds of cold metals.** **a** Crystal structures of four typical cold metals: ZrRuSb, RbCu<sub>4</sub>S<sub>3</sub>, CoSi, and Sr<sub>3</sub>Pb<sub>3</sub>F. Band structures, DOS, and phonon spectra:

**b** ZrRuSb, **c** RbCu<sub>4</sub>S<sub>3</sub>, **d** CoSi, and **e** Sr<sub>3</sub>Pb<sub>3</sub>F. The Fermi levels are set to zero. There is a band gap in the conduction band ( $E_{CG}$ ) or valence band ( $E_{VC}$ ) of these materials.

power factor (PF) of cold metals are compared with those of Cu, Co, and Ru in Fig. 4, which are used in the CMOS technology. We use the relaxation time of Cu, Co, and Ru in ref. 28 to evaluate the above properties<sup>28</sup>. All four cold metal materials are compounds and have an energy gap around the Fermi level. So, it is reasonable to observe that the conductance of these cold metals is smaller than that of traditional contact metals in Fig. 4a. CoSi has the largest conductance among the four cold metals. The thermal conductance of these cold metals is also smaller than those of traditional contact metals in Fig. 4b, which is beneficial for higher thermoelectric efficiency<sup>42</sup>. It is interesting that with the evaluation value of  $\tau = 30$  fs, ZrRuSb has a conductance as large as  $10^7$  S m<sup>-1</sup>. However, after considering the electron-phonon coupling to get the relaxation time, the conductance of ZrRuSb descends to  $2 \times 10^6$  S m<sup>-1</sup>. The change of the conductance indicates that the relaxation time is significant to evaluate the electronic and thermoelectric transport properties and the conductance calculated above is just an estimated value. In semiconductors, the Seebeck coefficient's absolute value usually reaches the maximum as the Fermi level is around the conduction band minimum (CBM) or valence band maximum (VBM) and then decreases as the increase of the energy difference between the Fermi level and CBM/VBM<sup>43</sup>. Cold metals can be viewed as highly doped n-type or p-type semiconductors and therefore have a larger Seebeck coefficient than conventional metals in Fig. 4c. Seebeck coefficients of all cold metals are larger than those of normal metals. While, cold materials of Sr<sub>3</sub>Pb<sub>3</sub>F have more significant Seebeck coefficients over  $30 \mu\text{V K}^{-1}$  at room temperature and  $80 \mu\text{V K}^{-1}$  at 1000 K as shown in Fig. 4c. The high Seebeck coefficients of cold metals result in larger  $zT$  than conventional metals by several orders of magnitude, as shown in Fig. 4e. The  $zT$  of Sr<sub>3</sub>Pb<sub>3</sub>F can reach 0.6 at 1000 K. Because of the high thermal conductance, metals may not get higher  $zT$  than semiconductors. However, benefit from the high conductance, metals have a

larger power factor than semiconductors. CoSi has a large power factor of nearly  $10 \text{ mW m}^{-1} \text{ K}^{-2}$  at 700 K as shown in Fig. 4d. Therefore, cold metals have more promising thermoelectric properties than normal metals and have an excellent potential for improving power dissipation in integrated circuits. Specifically, we studied the possibility of modulating the electronic properties of ZrRuSb by doping or changing the composition. It is found that the energy difference between the band gap edge and the Fermi level can be decreased in Zr<sub>3</sub>Ru<sub>3</sub>Sb<sub>7</sub>Te, Zr<sub>8</sub>Ru<sub>9</sub>Sb<sub>7</sub>, Zr<sub>8</sub>Ru<sub>9</sub>Sb<sub>5</sub>Te (see Supplementary Fig. 9), which is 0.42 eV, 0.40 eV and 0.33 eV, respectively. Our current approach involves electronic band structure and phonon spectrum calculations exclusively at 0 K. Temperature-dependent calculations offer a valuable avenue for achieving greater accuracy in determining the electronic and thermoelectric properties of cold metals.

### Cold metal for filtering high-energy carriers

Except for the thermoelectric properties, cold metals have already been proposed to filter high-energy carriers for steep switching because of the intrinsic band gap around the Fermi level. We first illustrate the mechanism of cold metal for injecting cold electrons. Figure 5a, b compares device structures of conventional metal oxide semiconductor field effect transistors (MOSFETs) and FETs with a cold metal contact. In conventional MOSFETs, electrons are injected from normal metals with a constant density of states (DOS) around the Fermi level as shown in Fig. 5c. Subthreshold swing (SS) can be derived as  $(k_B T/q) \times \ln 10$  and cannot be less than  $60 \text{ mV decade}^{-1}$  at room temperature due to the Boltzmann distribution, where  $k_B T$  is the thermal energy and  $q$  is the elemental charge. As the decreasing of temperature, the injected carrier distribution function is changed as shown in Fig. 5c. The slope of carrier distribution gets smaller as the temperature decreases from 300 K to 100 K and SS is effectively improved. When p-type

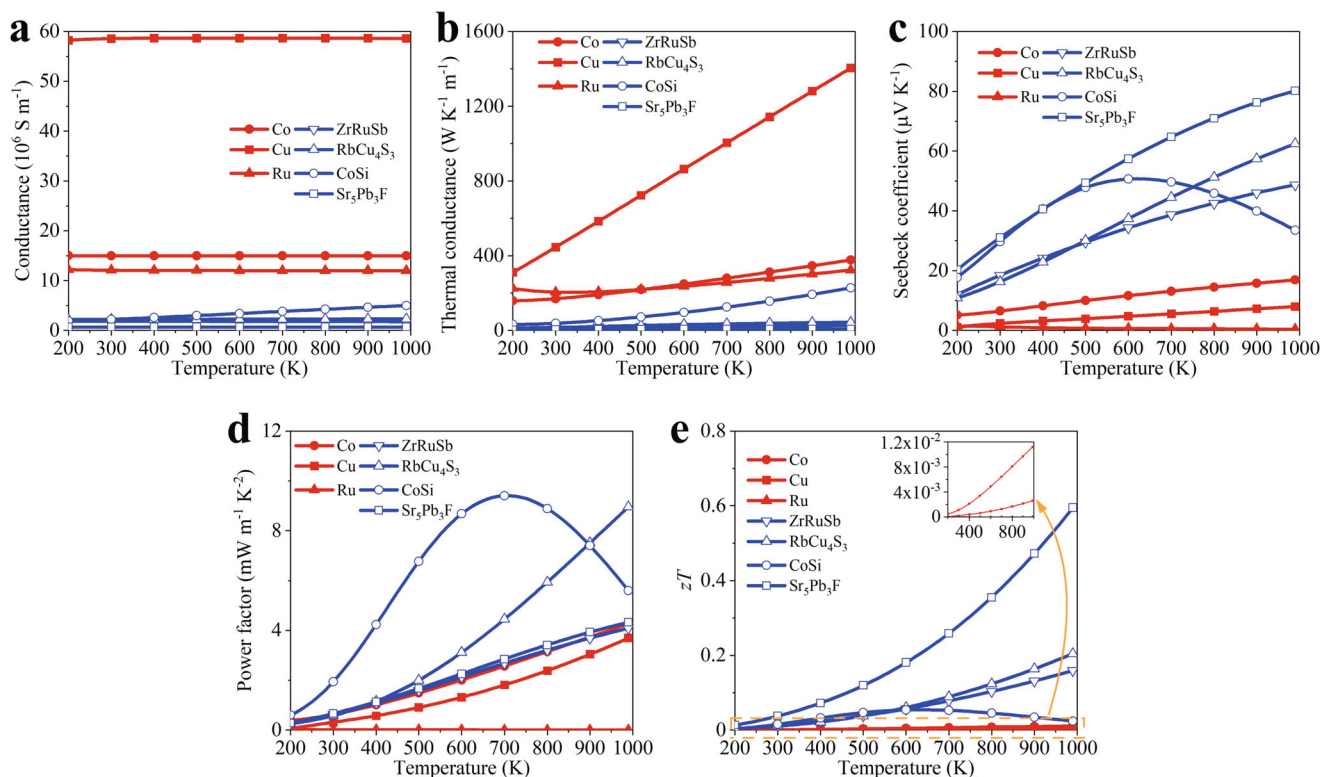


**Fig. 4 | Thermoelectric properties of cold metals and normal metals.**

**a** Conductance, **b** Thermal conductance, **c** Seebeck coefficient, **d** Power factor, **e**  $zT$ , of cold metals and normal metals. Normal metals such as Co, Cu, and Ru have larger

conductance. While, cold metals have lower thermal conductance and more significant Seebeck coefficients,  $zT$ s, and Power factor.

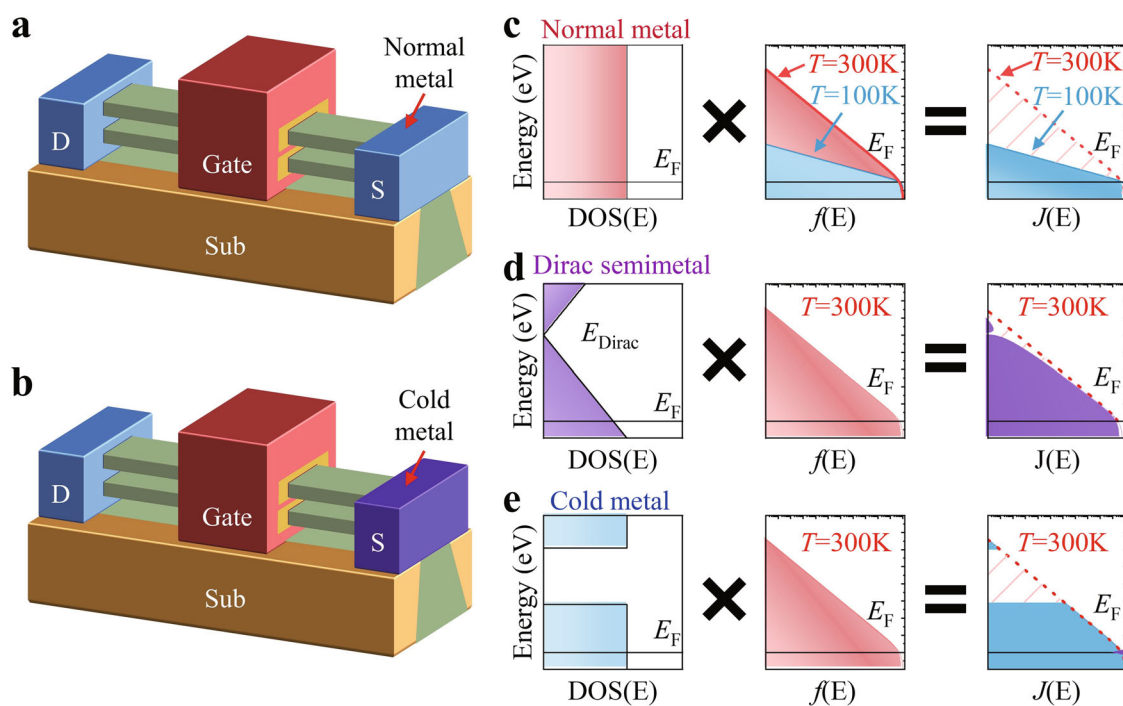


**Fig. 5 | Schematic device structure and switching mechanism of FET with a cold metal contact.** Schematic device structures of **a** conventional FET and **b** FET with a cold metal contact. The injected current density  $J(E)$  from **c** normal metal, **d** Dirac semimetal, and **e** cold metal, which is determined by the source DOS and the Fermi distribution function  $f(E)$  and given by  $J(E) \propto DOS(E) \times f(E)$ . **c** The subthreshold

swing is corresponding to the slope of  $J(E)$  and can be decreased by lowering the temperature in a FET using normal metal. **d** The slope of the injected current density is suppressed by the Dirac point. **e** SS can be further decreased by using a cold metal source with an energy gap above the Fermi level. There is an abrupt change in the injected current density, which is similar to the case at zero temperature.

graphene is applied as the injection source, the distribution of electrons gets super-exponential due to the linear DOS as shown in Fig. 5d. The slope of the distribution gets smaller, which corresponds to the decrease of the SS limit. So, graphene works as a cold source (CS) to inject cold electrons<sup>44,45</sup>. However, the Dirac source of graphene still has a finite slope of carrier distribution with an SS limit of 37 mV decade<sup>-1</sup>. A more effective way to reduce SS is to induce an energy gap above the Fermi level<sup>46</sup>, as plotted in Fig. 5e. The slope can be zero by using such a gapped source, which is the same as conventional MOSFETs at zero temperature. So, such a gapped source can more effectively filter high-energy electrons and achieve steeper switching. A gapped cold source can be realized using a p-type semiconductor<sup>44,46</sup>, or isolated electronic states<sup>47</sup>, which have to be doped. A much simpler device structure is to directly replace the metal contact with cold metals, as shown in Fig. 5b. For the materials we have calculated, ZrRuSb has an energy gap above the Fermi level and can be applied in n-type cold source field effect transistors (CSFETs). RbCu<sub>4</sub>S<sub>3</sub> and Sr<sub>5</sub>Pb<sub>3</sub>F also have an energy gap above the Fermi level and can be used in n-type CSFETs. While CoSi has a gap below the Fermi level and can be used in p-type CSFETs. These cold metals are 3D materials and can be directly used as an injection source in FETs to achieve steep slope switching.

**Cold source transistors with a cold metal contact**

At last, we studied the transport properties of CSFETs with a cold metal contact and particularly applied ZrRuSb as the injection source in monolayer MoS<sub>2</sub> transistors to realize steep slope switching. The atomistic contact between the cold metal of ZrRuSb and monolayer MoS<sub>2</sub> is shown in Fig. 6a, which is calculated by first-principles quantum transport simulations as implemented in Nanodcal software<sup>48</sup>. The interfacial structure is optimized by density functional theory (DFT) calculations and the energies of the interfacial structure plotted as the function of the physical separation are shown in Supplementary Fig. 10. Here, an edge contact covalently bonding with ML-MoS<sub>2</sub> is considered due to high orbital overlap<sup>49</sup>. Figure 6a shows

the projected local density of states (PLDOS) of the system calculated along the transport direction, which can demonstrate the band alignment of the heterostructure. The contact between ZrRuSb and intrinsic ML-MoS<sub>2</sub> is a Schottky type and the barrier height is about 0.7 eV. In order to reduce the contact resistance and realize cold electron injection, ML-MoS<sub>2</sub> has to be doped to n-type. As the increasing of the doping density, electrons can transport from ZrRuSb to the conduction band of ML-MoS<sub>2</sub> as indicated by the transmission around the Fermi energy of the cold metal in Fig. 6a. Because there is an energy gap above the Fermi level of ZrRuSb, those electrons in the energy region are filtered and cold electron injection is realized. The contact resistance is decreased to 13 Ω·μm as doping density reaches 5.67 × 10<sup>13</sup> cm<sup>-2</sup> in Fig. 6b, which is close to the contact resistance between Cu and MoS<sub>2</sub>.

The I<sub>D</sub>-V<sub>G</sub> curve of CSFET with ZrRuSb as the injection source at the ballistic transport limit can be simulated by using the transmission and the top-of-barrier model of MOSFET<sup>50</sup>. The transfer characteristic of ML-MoS<sub>2</sub> can be well calculated as benchmarking with the literature as shown in Supplementary Fig. 11. The device structure of CSFET is shown in Fig. 6c, comprising a gate oxide layer equivalent to 1 nm of SiO<sub>2</sub> and 10 nm gate length. The only difference between MOSFET and the proposed CSFET is replacing the conventional metal contact with cold metal. Figure 6d compares the I<sub>D</sub>-V<sub>G</sub> curves of the two devices by fixing the off-state current at 100 pA μm<sup>-1</sup> to meet the requirements of the International Roadmap for Devices and Systems (IRDS) 2021 for high-density (HD)<sup>51</sup>. The on-state current at V<sub>G</sub> = V<sub>D</sub> = 0.5 V is about 1.4 × 10<sup>3</sup> μA μm<sup>-1</sup> in CSFETs, which is much larger than 2.6 × 10<sup>2</sup> μA μm<sup>-1</sup> in MOSFET. To reach the same on-state current, V<sub>G</sub> has to be increased to 0.89 V in MOSFET. Therefore, the supply voltage is greatly decreased and power consumption can be significantly improved in CSFETs. With the obtained transmission, we can study the impact of the band gap edge of ZrRuSb on the device performance of CSFETs by shifting the Fermi level energy. It is found the switching properties can be improved as the energy difference E<sub>CD</sub> between the band gap

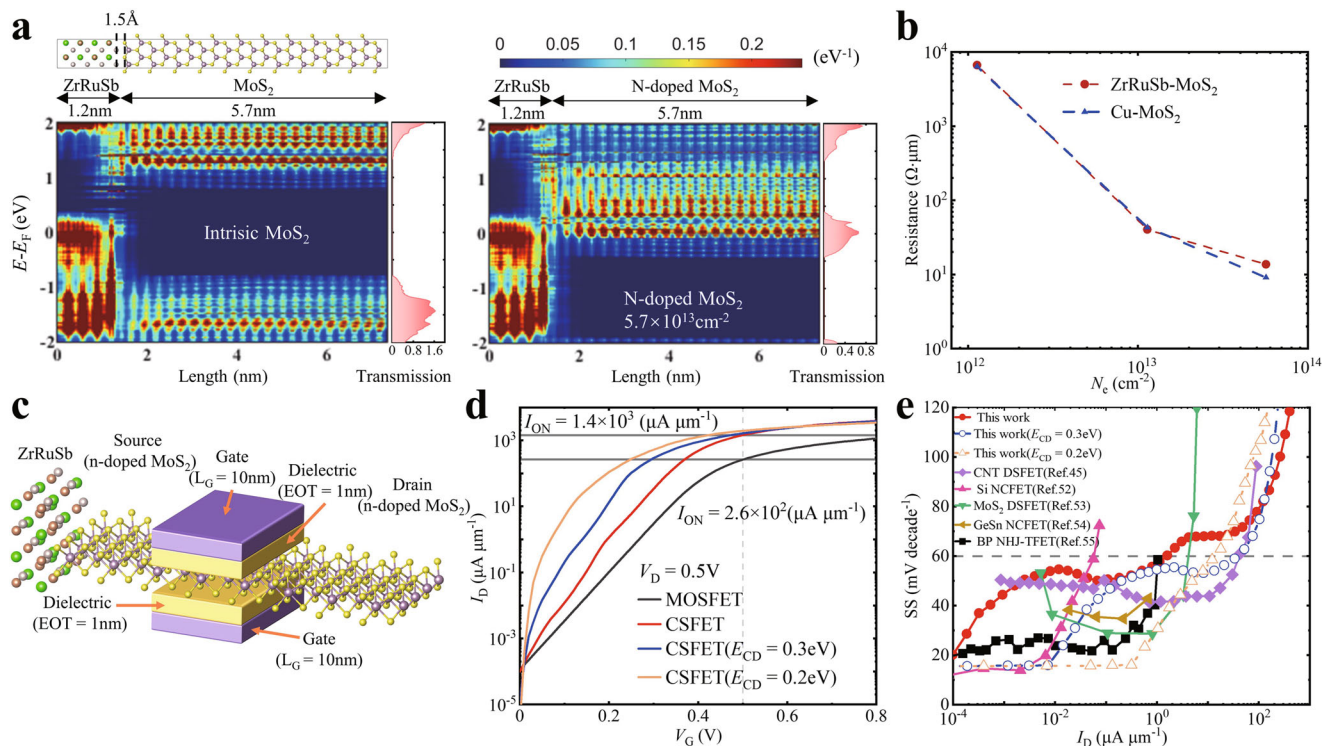


**Fig. 6 | Transport properties of the ZrRuSb-MoS<sub>2</sub> heterojunction.** **a** LDOS and transmissions of the ZrRuSb-MoS<sub>2</sub> heterojunction with intrinsic MoS<sub>2</sub> and n-type MoS<sub>2</sub>. The Schottky barrier height between ZrRuSb and MoS<sub>2</sub> can be reduced by increasing the doping density of MoS<sub>2</sub>. **b** Resistance vs MoS<sub>2</sub> doping concentration

of the ZrRuSb-MoS<sub>2</sub> heterojunction. **c** The device structure of MoS<sub>2</sub> CSFET with a ZrRuSb contact. **d** Transfer characteristics of MoS<sub>2</sub> FETs and CSFETs. **e** SS as a function of I<sub>D</sub>. The I<sub>60</sub> of this work at which SS reaches 60 mV decade<sup>-1</sup> is larger than 1 μA μm<sup>-1</sup>, which can be improved by modulating the E<sub>CD</sub>.

edge and the Fermi level is decreased. SS can be smaller than 20 mV decade<sup>-1</sup> over four decades at  $E_{CD} = 0.2$  eV in Fig. 6d. Figure 6e shows SS as a function of  $I_D$  of CSFETs compared with other steep slope devices<sup>45,52–55</sup>. The current  $I_{60}$  at which SS reaches 60 mV decade<sup>-1</sup> is about  $1 \mu\text{A} \mu\text{m}^{-1}$  in this work, larger than those of tunneling field effect transistors (TFETs)<sup>55</sup> and negative capacitance field effect transistors (NCFETs)<sup>52,54</sup>. The  $I_{60}$  of this work is smaller than that of Dirac source field effect transistors (DSFETs) because the  $E_{CD}$  of ZrRuSb is 0.42 eV which is too large to realize high  $I_{60}$  for CSFETs. The  $I_{60}$  of MoS<sub>2</sub> FETs with a ZrRuSb source contact can be further increased to be over  $10 \mu\text{A} \mu\text{m}^{-1}$  at  $E_{CD} = 0.2$  eV.

## Discussion

Theoretical exploration of cold metals is central to this study, yet the synthesis of these materials and the realization of device fabrication are pivotal for practical application. Achieving a single crystal phase in material synthesis is crucial to maintaining cold metal properties at room temperature. Given that cold metals are multicomponent compounds, ensuring compatibility with the semiconductor is essential during device fabrication. To optimize the performance of CSFETs with a cold metal electrode, achieving low contact resistance between the cold metals and the semiconductor is paramount. In the realm of 2D transistors, several methods such as van der Waals contacts<sup>56</sup> and an yttrium-doping-induced phase-transition<sup>57</sup> have been developed to reduce contact resistance. These methods can be adapted for achieving low contact resistance between cold metals and MoS<sub>2</sub>, thereby further enhancing CSFET performance.

In conclusion, 3D bulk cold metals are explored for electronic and thermoelectric devices. We performed a systematical material screening for 3D cold metals and found 252 kinds of bulk materials with an energy gap around the Fermi level. Detailed electronic and thermoelectric properties of cold metals are calculated by first-principles simulations. Cold metals have a much larger power factor and figure-of-merit than normal metals. The largest estimated  $zT$  can reach 0.6 at 1000 K. Besides, these materials have a great potential to replace conventional metal contact materials in transistors to realize sub-60 mV decade<sup>-1</sup> switching. These cold metals can effectively filter high-energy electrons as a cold electron injection source. Therefore, these materials are beneficial for reducing power dissipation in integrated circuits. We also show that cold metals can be applied as the injection source of MoS<sub>2</sub> FETs to achieve sub-60 mV decade<sup>-1</sup> switching over four decades and on-state current over  $10^3 \mu\text{A} \mu\text{m}^{-1}$ . Our work paves the way to realize steep slope and thermoelectric devices by using 3D cold metal contacts for low-power applications.

## Methods

### Density functional theory calculations

First principles calculations were performed using Vienna ab initio simulation package (VASP), in which the core-valence interaction is described by the projector-augmented-wave method<sup>58</sup>. The exchange-correlation function is treated by the Perdew-Burke-Ernzerh generalized gradient approximation<sup>59,60</sup>. The cutoff energy for plane-wave expansion was set as 520 eV. Monkhorst-Pack k-point meshes were used for sampling the Brillouin zone with a  $6 \times 6 \times 6$  grid for structure relaxations and  $9 \times 9 \times 9$  grid for self-consistent calculations. The structure relaxation was calculated until the residual force was less than  $0.01 \text{ eV} \text{ \AA}^{-1}$ . We calculated a  $2 \times 2 \times 2$  supercell of ZrRuSb and changed one atom to simulate the doping. The cutoff energy for plane-wave expansion was set as 500 eV for structure relaxations and 450 eV for self-consistent calculations. A  $9 \times 9 \times 9$  grid was used for the Brillouin-zone sampling. The thermoelectric properties were calculated by BoltzTraP2, which used the eigenvalues calculated by VASP with a  $15 \times 15 \times 15$  k-point mesh. The relaxation time is calculated by EPW code within Quantum ESPRESSO<sup>38,39</sup>. The work function was determined using VASP by incorporating a vacuum layer larger than  $15 \text{ \AA}$  in a thin film. The vacuum energy level is confirmed by analyzing the electric potential across the thin film. The difference between the vacuum level and the Fermi level defines the work function. The band alignment can be derived by comparing the

extracted work functions. For the calculation of magnetism, we set the initial magnetic moment as 1.0 for every atom.

### Phonon calculations

Phonon calculations were completed using the finite displacement method implemented in phonopy<sup>61</sup>. The cutoff energy for plane-wave expansion was set as 500 eV. For the  $2 \times 2 \times 2$  supercell of these four materials, we used a  $5 \times 5 \times 5$  grid for sampling the Brillouin zone. The energy convergence criteria were set at  $10^{-8}$  eV. The lattice thermal conductivity was calculated with phono3py<sup>40,41</sup>.

### Contact calculations

The contact structure between ZrRuSb and MoS<sub>2</sub> was optimized by minimizing the total energy by DFT calculations using VASP. Reasonable structure is significant for heterojunction calculation. For a smaller mismatch, we choose the (100) face of ZrRuSb to contact with MoS<sub>2</sub>. ZrRuSb has two kinds of (100) faces. One of them is Ru face and the other is Zr-Rb face. To determine the structure, we calculate several structures of the ZrRuSb and MoS<sub>2</sub> heterojunction with different physical separations. The total energies are plotted as the function of the physical separation as shown in Supplementary Fig. 10. The Ru interface of ZrRuSb and MoS<sub>2</sub> have the lowest value with a distance of  $1.5 \text{ \AA}$ . After getting the structure with the lowest energy, we performed a relaxation with VASP to get a reasonable result to calculate the transport properties. The transport properties of the heterojunction were calculated using the Nanodcal software based on the non-equilibrium Green's function (NEGF) method in combination with DFT<sup>48</sup>. We used a  $5 \times 15 \times 1$  grid for Brillouin-zone sampling and 100 Hartree density for the mesh cutoff. The heterojunction consists of 1.2 nm ZrRuSb and 5.9 nm MoS<sub>2</sub>. Carrier doping of MoS<sub>2</sub> is treated by the virtual crystal approximation.

### Data availability

The data that support the findings of this study are available from the corresponding author upon reasonable request. The structures of 30 kinds of cold metals are available (<https://github.com/PKU-LG-Zhang/MP-structure>).

Received: 26 June 2023; Accepted: 10 April 2024;

Published online: 22 April 2024

## References

- Brain, R. in *Proc. 2016 IEEE International Electron Devices Meeting (IEDM)* 9.3.1–9.3.4 (IEEE, 2016).
- Gall, D. et al. Materials for interconnects. *MRS Bull.* **46**, 959–966 (2021).
- Geim, A. K. Graphene: status and prospects. *Science* **324**, 1530–1534 (2009).
- Manzeli, S., Ovchinnikov, D., Pasquier, D., Yazyev, O. V. & Kis, A. 2D transition metal dichalcogenides. *Nat. Rev. Mater.* **2**, 1–15 (2017).
- Anasori, B., Lukatskaya, M. R. & Gogotsi, Y. 2D metal carbides and nitrides (MXenes) for energy storage. *Nat. Rev. Mater.* **2**, 1–17 (2017).
- Zhou, Y. et al. Tensile strain switched ferromagnetism in layered NbS<sub>2</sub> and NbSe<sub>2</sub>. *Acs Nano* **6**, 9727–9736 (2012).
- Liu, F. Switching at less than 60 mV/decade with a “cold” metal as the injection source. *Phys. Rev. Appl.* **13**, 064037 (2020).
- Wang, Z. et al. Cold source diodes with sub-unity ideality factor and giant negative differential resistance. *IEEE Electron Device Lett.* **43**, 2184–2187 (2022).
- Yin, Y. et al. Negative differential resistance effect in “Cold” metal heterostructure diodes. *IEEE Electron Device Lett.* **43**, 498–501 (2022).
- Şaşıoğlu, E. & Mertig, I. Theoretical prediction of semiconductor-free negative differential resistance tunnel diodes with high peak-to-valley current ratios based on two-dimensional cold metals. *ACS Appl. Nano Mater.* **6**, 3758–3766 (2023).

11. Rasmussen, F. A. & Thygesen, K. S. Computational 2D materials database: electronic structure of transition-metal dichalcogenides and oxides. *J. Phys. Chem. C* **119**, 13169–13183 (2015).
12. Snyder, G. J. & Toberer, E. S. Complex thermoelectric materials. *Nat. Mater.* **7**, 105–114 (2008).
13. Yan, Q. & Kanatzidis, M. G. High-performance thermoelectrics and challenges for practical devices. *Nat. Mater.* **21**, 503–513 (2022).
14. Gramroudi, F. et al. High thermoelectric performance in metallic NiAu alloys via interband scattering. *Sci. Adv.* **9**, eadj1611 (2023).
15. Mahan, G. D. & Sofo, J. O. The best thermoelectric. *Proc. Natl Acad. Sci. USA* **93**, 7436 (1996).
16. Wickramaratne, D., Zahid, F. & Lake, R. K. Electronic and thermoelectric properties of few-layer transition metal dichalcogenides. *J. Chem. Phys.* **140**, 124710 (2014).
17. Ashton, M., Paul, J., Sinnott, S. B. & Hennig, R. G. Topology-scaling identification of layered solids and stable exfoliated 2D materials. *Phys. Rev. Lett.* **118**, 106101 (2017).
18. Sendek, A. D. et al. Holistic computational structure screening of more than 12000 candidates for solid lithium-ion conductor materials. *Energy Environ. Sci.* **10**, 306–320 (2017).
19. Mounet, N. et al. Two-dimensional materials from high-throughput computational exfoliation of experimentally known compounds. *Nat. Nanotechnol.* **13**, 246–252 (2018).
20. Zhu, Y., Kong, X., Rhone, T. D. & Guo, H. Systematic search for two-dimensional ferromagnetic materials. *Phys. Rev. Mater.* **2**, 081001 (2018).
21. Zhang, T. et al. Catalogue of topological electronic materials. *Nature* **566**, 475–479 (2019).
22. Osanloo, M. R., Van de Put, M. L., Saadat, A. & Vandenberghe, W. G. Identification of two-dimensional layered dielectrics from first principles. *Nat. Commun.* **12**, 1–8 (2021).
23. Jain, A. et al. Commentary: The Materials Project: A materials genome approach to accelerating materials innovation. *APL Mater.* **1**, 011002 (2013).
24. Kresse, G. & Furthmüller, J. Efficient iterative schemes for ab initio total-energy calculations using a plane-wave basis set. *Phys. Rev. B* **54**, 11169 (1996).
25. Kresse, G. & Joubert, D. From ultrasoft pseudopotentials to the projector augmented-wave method. *Phys. Rev. B* **59**, 1758 (1999).
26. Madsen, G. K., Carrete, J. & Verstraete, M. J. BoltzTraP2, a program for interpolating band structures and calculating semi-classical transport coefficients. *Comput. Phys. Commun.* **231**, 140–145 (2018).
27. Mustafa, J. I., Bernardi, M., Neaton, J. B. & Louie, S. G. Ab initio electronic relaxation times and transport in noble metals. *Phys. Rev. B* **94**, 155105 (2016).
28. Gall, D. Electron mean free path in elemental metals. *J. Appl. Phys.* **119**, 085101 (2016).
29. Evers, C. B., Richter, C. G., Hartjes, K. & Jeitschko, W. Ternary transition metal antimonides and bismuthides with MgAgAs-type and filled NiAs-type structure. *J. Alloy. Compd.* **252**, 93–97 (1997).
30. Folmer, J. & Jellinek, F. The valence of copper in sulphides and selenides: An X-ray photoelectron spectroscopy study. *J. Less Common Met.* **76**, 153–162 (1980).
31. Demchenko, P. et al. Single crystal investigation of the new phase Er<sub>0.85</sub>Co<sub>4.31</sub>Si and of CoSi. *Chem. Met. Alloys*, **1**, 50–53 (2008).
32. Leon-Escamilla, E. A. & Corbett, J. D. Hydrogen impurity effects. A<sub>5</sub>Tt<sub>3</sub>Z intermetallic compounds between A= Ca, Sr, Ba, Eu, Yb and Tt= Sn, Pb with Cr<sub>5</sub>B<sub>3</sub>-like structures that are stabilized by hydride or Fluoride (Z). *Inorg. Chem.* **40**, 1226–1233 (2001).
33. Jung, D., Koo, H.-J. & Whangbo, M.-H. Study of the 18-electron band gap and ferromagnetism in semi-Heusler compounds by non-spin-polarized electronic band structure calculations. *J. Mol. Struct.* **527**, 113–119 (2000).
34. Casper, F., Graf, T., Chadov, S., Balke, B. & Felser, C. Half-Heusler compounds: novel materials for energy and spintronic applications. *Semicond. Sci. Technol.* **27**, 063001 (2012).
35. Wen, X.-D., Martin, R. L., Henderson, T. M. & Scuseria, G. E. Density functional theory studies of the electronic structure of solid-state actinide oxides. *Chem. Rev.* **113**, 1063–1096 (2013).
36. Kudin, K. N., Scuseria, G. E. & Martin, R. L. Hybrid density-functional theory and the insulating gap of UO<sub>2</sub>. *Phys. Rev. Lett.* **89**, 266402 (2002).
37. Gao, W. et al. On the applicability of hybrid functionals for predicting fundamental properties of metals. *Solid State Commun.* **234**, 10–13 (2016).
38. Giustino, F., Cohen, M. L. & Louie, S. G. Electron-phonon interaction using Wannier functions. *Phys. Rev. B* **76**, 165108 (2007).
39. Giannozzi, P. et al. Advanced capabilities for materials modelling with Quantum ESPRESSO. *J. Phys. Condens. Matter* **29**, 465901 (2017).
40. Togo, A., Chaput, L. & Tanaka, I. Distributions of phonon lifetimes in Brillouin zones. *Phys. Rev. B* **91**, 094306 (2015).
41. Togo, A., Chaput, L., Tadano, T. & Tanaka, I. Implementation strategies in phonopy and phono3py. *J. Phys. Condens. Matter* **35**, 353001 (2023).
42. Zeier, W. G. et al. Engineering half-Heusler thermoelectric materials using Zintl chemistry. *Nat. Rev. Mater.* **1**, 1–10 (2016).
43. Maassen, J. & Lundstrom, M. A computational study of the thermoelectric performance of ultrathin Bi<sub>2</sub>Te<sub>3</sub> films. *Appl. Phys. Lett.* **102**, 093103 (2013).
44. Liu, F. et al. Dirac electrons at the source: Breaking the 60-mV/decade switching limit. *IEEE Trans. Electron Devices* **65**, 2736–2743 (2018).
45. Qiu, C. et al. Dirac-source field-effect transistors as energy-efficient, high-performance electronic switches. *Science* **361**, 387–392 (2018).
46. Liu, F. et al. in *Proc. 2018 IEEE International Electron Devices Meeting (IEDM)* 33.32.31–33.32.34 (IEEE, 2018).
47. Wang, Q. et al. Strain engineered C<sub>31</sub> field-effect-transistors: a new strategy to break 60 mV/decade by using electron injection from intrinsic isolated states. *Appl. Phys. Express* **14**, 074003 (2021).
48. Taylor, J., Guo, H. & Wang, J. Ab initio modeling of quantum transport properties of molecular electronic devices. *Phys. Rev. B* **63**, 245407 (2001).
49. Allain, A., Kang, J., Banerjee, K. & Kis, A. Electrical contacts to two-dimensional semiconductors. *Nat. Mater.* **14**, 1195–1205 (2015).
50. Rahman, A., Guo, J., Datta, S. & Lundstrom, M. S. Theory of ballistic nanotransistors. *IEEE Trans. Electron Devices* **50**, 1853–1864 (2003).
51. *IEEE International Roadmap for Devices and Systems*. <https://irds.ieee.org/editions> (2021).
52. Liu, C. et al. in *Proc. 2019 Symposium on VLSI Technology T224–T225* (IEEE, 2019).
53. Liu, M. et al. in *Proc. 2020 IEEE International Electron Devices Meeting (IEDM)* 12.15.11–12.15.14 (IEEE, 2020).
54. Zhou, J. et al. Ferroelectric negative capacitance GeSn PFETs with sub-20 mV/decade subthreshold swing. *IEEE Electron Device Lett.* **38**, 1157–1160 (2017).
55. Kim, S. et al. Thickness-controlled black phosphorus tunnel field-effect transistor for low-power switches. *Nat. Nanotechnol.* **15**, 203–206 (2020).
56. Wang, Y. et al. Van der Waals contacts between three-dimensional metals and two-dimensional semiconductors. *Nature* **568**, 70–74 (2019).
57. Jiang, J., Xu, L., Qiu, C. & Peng, L.-M. Ballistic two-dimensional InSe transistors. *Nature* **616**, 470–475 (2023).
58. Blöchl, P. E. Projector augmented-wave method. *Phys. Rev. B* **50**, 17953 (1994).
59. Perdew, J. P., Burke, K. & Ernzerhof, M. Generalized gradient approximation made simple. *Phys. Rev. Lett.* **77**, 3865 (1996).
60. Grimme, S. Semiempirical GGA-type density functional constructed with a long-range dispersion correction. *J. Comput. Chem.* **27**, 1787–1799 (2006).
61. Togo, A. & Tanaka, I. First principles phonon calculations in materials science. *Scr. Mater.* **108**, 1–5 (2015).



## Acknowledgements

F.L. acknowledges support from NSFC (Grant nos. T2293703, T2293700, and 61974003) and the 111 Project (Grant no. B18001).

## Author contributions

F. L. conceived and supervised the project. L.Z. developed the theoretical model and performed device simulations. F.L. and L.Z. wrote the manuscript. All the authors contribute to editing the manuscript.

## Competing interests

The authors declare no competing interests.

## Additional information

**Supplementary information** The online version contains

supplementary material available at

<https://doi.org/10.1038/s41524-024-01267-w>.

**Correspondence** and requests for materials should be addressed to Fei Liu.

**Reprints and permissions information** is available at

<http://www.nature.com/reprints>

**Publisher's note** Springer Nature remains neutral with regard to jurisdictional claims in published maps and institutional affiliations.

**Open Access** This article is licensed under a Creative Commons Attribution 4.0 International License, which permits use, sharing, adaptation, distribution and reproduction in any medium or format, as long as you give appropriate credit to the original author(s) and the source, provide a link to the Creative Commons licence, and indicate if changes were made. The images or other third party material in this article are included in the article's Creative Commons licence, unless indicated otherwise in a credit line to the material. If material is not included in the article's Creative Commons licence and your intended use is not permitted by statutory regulation or exceeds the permitted use, you will need to obtain permission directly from the copyright holder. To view a copy of this licence, visit <http://creativecommons.org/licenses/by/4.0/>.

© The Author(s) 2024